

Viscosity of confined inhomogeneous nonequilibrium fluids

Junfang Zhang and B. D. Todd^{a)}

Centre for Molecular Simulation, Swinburne University of Technology, Hawthorn, Victoria 3122, Australia

Karl P. Travis

Immobilisation Science Laboratory, Department of Engineering Materials, University of Sheffield, Sheffield S1 3JD, United Kingdom

(Received 22 July 2004; accepted 1 September 2004)

We use the nonlocal linear hydrodynamic constitutive model, proposed by Evans and Morriss [Statistical Mechanics of Nonequilibrium Liquids (Academic, London, 1990)], for computing an effective spatially dependent shear viscosity of inhomogeneous nonequilibrium fluids. The model is applied to a simple atomic fluid undergoing planar Poiseuille flow in a confined channel of several atomic diameters width. We compare the spatially dependent viscosity with a local generalization of Newton's law of viscosity and the Navier–Stokes viscosity, both of which are known to suffer extreme inaccuracies for highly inhomogeneous systems. The nonlocal constitutive model calculates effective position dependent viscosities that are free from the notorious singularities experienced by applying the commonly used local constitutive model. It is simple, general, and has widespread applicability in nanofluidics where experimental measurement of position dependent transport coefficients is currently inaccessible. In principle the method can be used to predict approximate flow profiles of any arbitrary inhomogeneous system. We demonstrate this by predicting the flow profile for a simple fluid undergoing planar Couette flow in a confined channel of several atomic diameters width. © 2004 American Institute of Physics. [DOI: 10.1063/1.1809582]

I. INTRODUCTION

The properties of confined fluids can differ markedly from those of the corresponding bulk fluid. These differences arise from the competition between the interatomic forces operating between fluid atoms, and the interatomic forces acting between fluid atoms and the atoms constituting the confining material. This competition can lead to the formation of a nonuniform fluid density profile, a shift in the thermodynamic equilibrium properties and a modification of the transport properties. In particular, a nonuniform density profile results in spatial inhomogeneities in all transport properties.^{1–9} When the fluid is driven away from thermodynamic equilibrium, either by some external force (such as gravity or a pressure head) or by boundary conditions (e.g., Couette flow), the transport properties become functions of the local thermodynamic state variables as well as explicit functions of the thermodynamic driving field. Couplings may occur between thermodynamic forces sharing the same tensorial character adding further to the complexity.^{10–12}

A central problem in the study of confined fluids is the computation of meaningful transport coefficients. For confined fluids undergoing flow at low Reynolds number, classical Navier–Stokes hydrodynamic theory adequately describes the rheological properties of the fluid, provided the length scale of the confinement is much greater than the dimension of the fluid molecules. However, once the confinement approaches molecular dimensions, Navier–Stokes theory must be generalized to allow for local, position de-

pendent transport coefficients. Computer simulations of simple fluids undergoing planar Poiseuille flow have demonstrated the validity of the local generalization of Navier–Stokes hydrodynamics.¹³ However, very careful simulations at quite high confinement of the order of 5 atomic diameters or less, have shown that even the local generalization becomes invalid at this length scale.^{14,15} A *local* shear viscosity for instance, relates the local strain rate at a point in the fluid to the local stress at the *same* point. In the simulations (which used nonequilibrium molecular dynamics, NEMD) it was possible to obtain both stress and strain rate profiles with high spatial resolution without any assumptions being made regarding the transport coefficients. The ratio of these two quantities was then used to *calculate* a shear viscosity. At very high degrees of confinement, the strain rate profile contained zeros resulting from stationary points in the fluid velocity profile. The stress profile, on the other hand, contained only one zero, located at the midpoint of the channel. Clearly, a viscosity obtained from the ratio of these quantities will involve singularities. This unsatisfactory result suggests further generalization of Navier–Stokes hydrodynamics is necessary. The need for an improved hydrodynamic theory is paramount given the increasing drive towards nanoscale technologies and applications such as nanofluidics, and the need for a unified theory of liquids, able to describe phenomena occurring at all length and time scales. Experimental results involving surface force apparatus¹⁶ indicate that very thin fluid films exhibit unusually high viscosities under confinement. An explanation for this phenomenon remains elusive.

Equilibrium and nonequilibrium molecular simulations of nanofluids have continued to escalate since the pioneering

^{a)}Author to whom correspondence should be addressed; Electronic mail: btodd@swin.edu.au

work done in the 1980s. However in most of these simulations the viscosity was only treated heuristically, often computing effective viscosities based on local measures rather than a genuine nonlocal viscosity.^{7,8}

The first statistical mechanics theory that rigorously attempted to solve this problem for nonequilibrium fluids was the Enskog-type theory of Davis.^{1,2} While successful, it was limited to the case of unidirectional inhomogeneity and several other approximations, such as the substitution of the pair correlation function for the inhomogeneous fluid by a corresponding function for the homogeneous fluid at a smoothed density. This work was later extended by Pozhar and Gubbins^{17–19} who developed a theory of transport, again based on a modified Enskog theory for inhomogeneous fluids.²⁰ The major limitation to this theory is that it relates local values of transport coefficients to integrals over equilibrium inhomogeneous singlet and pair correlation functions. It is unlikely that the theory will hold when systems are far from equilibrium. A comparison of the Pozhar–Gubbins (PG) theory was made with nonequilibrium molecular dynamics (NEMD) simulations of a fluid undergoing planar Poiseuille flow.²¹ However, the computation of local NEMD viscosities, defined as the ratio of the shear stress to the strain rate, was already known to be a severe approximation, leading to poor statistical accuracy as the strain rate approaches zero.

Some time ago it was suggested that the linear constitutive relations could be further generalized by invoking nonlocal transport coefficients.¹³ The nonlocal generalization of Newton's law of viscosity is then

$$P_{yx}(\mathbf{r}, t) = - \int_0^t ds \int_{-\infty}^{\infty} d\mathbf{r}' \eta(\mathbf{r} - \mathbf{r}', t - s) \dot{\gamma}(\mathbf{r}', s), \quad (1)$$

where η and $\dot{\gamma}$ are the shear viscosity kernel and strain rate, respectively, and we have ignored any explicit dependencies of these quantities on the local, intensive, thermodynamic state variables. Though not stated by Evans and Morriss,¹³ this form of the expression is exactly valid only for a system which is homogeneous in space because there is no explicit density dependence in the viscosity kernel. However, for systems that are strongly inhomogeneous the viscosity kernel should be written as $\eta(\mathbf{r}, \mathbf{r} - \mathbf{r}', t - s)$ or just $\eta(\mathbf{r}, \mathbf{r}', t - s)$. However, as yet there is no clear way to extract this viscosity kernel for an inhomogeneous system such as fluids in nanopores, and so in what follows we drop the explicit \mathbf{r} dependence. In this case the viscous kernel represents an effective (density averaged) viscosity density which when integrated over all space will provide an effective pore viscosity. In Sec. VI we will show that this effective viscosity density allows us to predict approximate flow profiles for inhomogeneous systems that are similar to what one would find in real nanofluidic systems.

In Eq. (1) the simple proportionality between stress and strain rate implicit in Newton's law and its local generalization has been replaced by a double convolution in space and time so that the stress at position \mathbf{r} and time t is not simply proportional to the strain rate at position \mathbf{r} and time t , but is proportional to the entire strain rate history, and strain rate

distribution across the fluid. What this means in practical terms is that all liquids have a memory effect and therefore behave viscoelastically.

At first sight, Eq. (1) appears somewhat unhelpful. However, in $\mathbf{k}\omega$ space, the double convolution becomes algebraic,²²

$$\tilde{P}_{yx}(\mathbf{k}, \omega) = - \tilde{\eta}(\mathbf{k}, \omega) \tilde{\gamma}(\mathbf{k}, \omega), \quad (2)$$

where the tildes denote the Fourier–Laplace transform of a function defined for an arbitrary function $A(\mathbf{r}, t)$ by

$$\tilde{A}(\mathbf{k}, \omega) = \int_0^{\infty} dt \int_{-\infty}^{\infty} d\mathbf{r} \exp[-i(\mathbf{k} \cdot \mathbf{r} + \omega t)] A(\mathbf{r}, t). \quad (3)$$

If the strain rate does not vary appreciably in time compared with the time scale for molecular motions, the zero frequency limit of Eq. (2) may be taken, giving

$$\tilde{P}_{xy}(\mathbf{k}) = - \tilde{\eta}(\mathbf{k}) \tilde{\gamma}(\mathbf{k}), \quad (4)$$

where the missing frequency arguments imply $\omega=0$. Equation (4), which defines the wave-vector-dependent viscosity, has been used previously to extract this quantity for bulk inhomogeneous fluids via the sinusoidal transverse force (STF) method.²³ In the STF method the inhomogeneities are introduced artificially via a sinusoidally varying external field which gives rise to an oscillatory density profile.

In the case of a homogeneous fluid we can represent the viscous kernel as $\eta(\mathbf{r} - \mathbf{r}') \equiv \eta \delta(\mathbf{r} - \mathbf{r}')$, where η is a constant. The spatial localization is introduced into Eq. (1) by means of the delta function. It is clear that for a spatially homogeneous system Eq. (1) simply reduces to the Navier–Stokes shear viscosity, as expected, i.e., $P_{yx}(\mathbf{r}) = - \eta \dot{\gamma}(\mathbf{r})$.

We have previously suggested^{14,21} that Eq. (4) could also be used to extract the viscosity from simulations of liquid flow through porous solids in which the degree of confinement meant that the local constitutive relation for viscosity was invalid. It was conjectured that if the strain rate and stress profiles could be obtained with sufficient spatial resolution and with high signal to noise, a wave-vector-dependent viscosity could be calculated from the Fourier transformed data via Eq. (4). A position dependent viscosity or viscosity profile could then be obtained via an inverse transform. Up until now, all attempts to verify this suggestion have ended in failure due to either insufficient accuracy in the profiles or a failure to appreciate some of the subtleties involved in evaluating the nonlocal viscosity. In this paper we outline a method for evaluating this quantity and, for the first time, demonstrate conclusively that the method works by computing the effective viscosity density of a highly confined simple fluid in which the local constitutive relation is invalid.

The remainder of the paper is set out as follows. In Sec. II we revise the Navier–Stokes theory for our simulation geometry; in Sec. III we describe the numerical details of the extraction of the viscous kernel in Eq. (1); in Sec. IV we give specific details of the simulations; in Sec. V we present the results and discuss them at length; in Sec. VI we describe how the effective position dependent viscosity density may

be used to predict approximate flow profiles for nanoscale flows with arbitrary geometry; while in Sec. VII we form some conclusions.

II. NAVIER–STOKES THEORY FOR FLUIDS IN SLIT PORES

The momentum continuity equation describing the flow of a single component fluid under the influence of an external field per unit mass, F_e , is given by

$$\rho \frac{du_x(y)}{dt} = - \frac{dP_{yx}(y)}{dy} + \rho F_e, \quad (5)$$

where ρ is the mass density, P_{yx} is the yx component of the viscous pressure tensor and the confinement is in the y direction while the external field acts in the x direction. This equation is valid arbitrarily far from equilibrium. The corresponding Navier–Stokes equation is then obtained by substituting Newton’s law of viscosity

$$P_{yx} = - \eta \dot{\gamma} \quad (6)$$

into the fluid equation of motion, and noting that in the steady state $du_x(y)/dt = 0$, i.e.,

$$\eta \frac{d\dot{\gamma}(y)}{dy} + \rho F_e = 0. \quad (7)$$

The Navier–Stokes equation is trivial to solve for the one-component fluid subject to gravity flow in a planar channel. Two key assumptions must be made however. The first is that the density is uniform throughout the fluid. The second assumption refers to the boundary conditions. A common boundary condition is the stick boundary condition (no slip) which states that the x component of velocity must vanish at the walls, i.e., $u_x(y = \pm h)$, where h is the distance from the center of the channel to the walls. With these assumptions, the solution for the streaming velocity is

$$u_x(y) = - \frac{h^2 \rho F_e}{2 \eta} (\bar{y}^2 - 1), \quad (8)$$

where $\bar{y} = y/h$.

The form of the streaming velocity can alternatively be determined from NEMD simulations of simple fluids undergoing Poiseuille flow. Here, the local velocity is obtained from its definition

$$\mathbf{J} = \rho \mathbf{u}, \quad (9)$$

where \mathbf{J} is the momentum density, and no assumptions are made in this case. The momentum and mass densities are obtained using their microscopic definitions,

$$J_x(y) = \frac{1}{A} \sum_i m_i v_{xi} \delta(y - y_i), \quad (10)$$

$$\rho(y) = \frac{1}{A} \sum_i m_i \delta(y - y_i), \quad (11)$$

with the Dirac delta functions replaced by functions which are finite in some small region of y , i.e., the data is simply collected in bins of thickness Δy and area A in the xz plane. Here m_i and v_i are the mass and velocity of particle i , re-

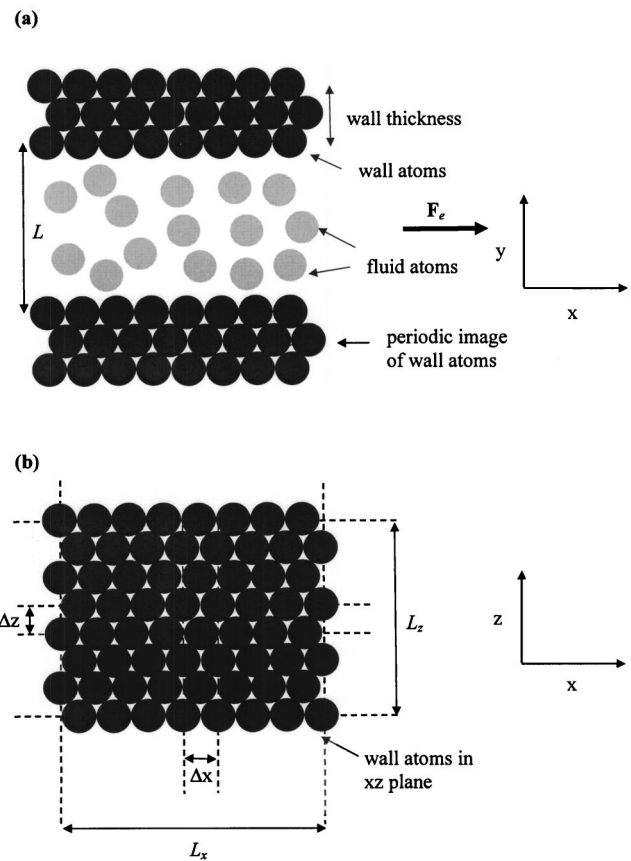


FIG. 1. Geometry of the simulation environment. (a) Overall system including fluid and wall atoms (z -direction normal to page); (b) wall atoms in the xz plane, defining separation of layers (y -direction normal to page).

spectively. Comparison of the simulated streaming velocity profiles with that predicted by Eq. (8) gives an indication of the accuracy of Navier–Stokes theory for high degrees of confinement. The authors and collaborators^{14,15,24} have made these comparisons and determined that for channels of the order of 10 atomic diameters in width or more, the Navier–Stokes predictions are largely correct if one allows for some slip at the walls. Below these pore widths, the velocity profiles develop some fine structure.

The viscosity can be determined within the NEMD simulations if one assumes a form for the constitutive relation. No other assumptions are made. The pressure tensor can be obtained by direct integration of the density profile followed by multiplication by the field magnitude, while the strain rate profile can be obtained by the numerical differentiation of the streaming velocity data (or, alternatively, by analytic differentiation of a functional fit to the velocity data). Departure from the quadratic behavior depicted by Eq. (8) indicates the limitations of assuming Newton’s law of viscosity, while a viscosity which is not uniformly finite implies the breakdown of assuming the more generalized local version of Newton’s law.

III. EXTRACTION OF VISCOUS KERNEL

Our approach is to conduct a series of NEMD simulations of a WCA fluid undergoing Poiseuille flow (details given in next section) at several pore widths. We have cal-

culated stress, velocity, and strain rate profiles with high numerical precision and with high spatial resolution in order to show that Eq. (4) is the correct generalization of Newton's law of viscosity. We note that for our geometry in the steady state (see Fig. 1), Eq. (1) reduces to $P_{yx}(y) = -\int_{-\infty}^{\infty} dy' \eta(y-y') \dot{\gamma}(y')$.

We apply numerical Fourier transforms and inverse Fourier transforms to all our data. The discrete Fourier transform is defined as²⁵

$$\tilde{F}\left(\frac{2n\pi}{NT_S}\right) = T_S \sum_{k=0}^{N-1} f(kT_S) e^{-2nk\pi i/N} \quad (12)$$

where $k, n=0,1,2,\dots,N-1$, N is the number of sampling points, and T_S is the sampling period. Here $f(\dots)$ denotes a function in \mathbf{r} space and $\tilde{F}(\dots)$ is its Fourier transform. The inverse discrete Fourier transform is given as

$$f(kT_S) = \frac{1}{NT_S} \sum_{n=0}^{N-1} \tilde{F}\left(\frac{2n\pi}{NT_S}\right) e^{2nk\pi i/N}. \quad (13)$$

It is important to appreciate that although our data is finite in space (i.e., there are only a finite number of bins in which we accumulate data) the infinite range taken in the limits of the integral in Eq. (1) appears in our numerical convolution via the periodic boundary conditions. For example, consider a simulation consisting of data contained within a total of n bins, ranging in bin number from 1 to n . What should the convoluted shear stress, defined by Eq. (1), be in bin number i ? Using a discretised version of Eq. (1) (assuming the zero frequency limit is taken) one finds

$$P_{yxi} = -\Delta y_{bin} \sum_{j=1}^n \eta_{i-j} \dot{\gamma}_j, \quad (14)$$

where $-P_{yxi}$ is the shear stress in the i th bin and Δy_{bin} is the bin width. As there are no bin numbers ≤ 0 we use periodic boundary conditions $\eta_{1-i} = \eta_{1-i+n}$ ($i=1,2,\dots,n$) to take all bins into account. Periodic boundary conditions are essential because our simulation is spatially periodic in y (it is also periodic in x and z). Failure to include these transformations in the convolution integral results in an erroneous convoluted stress.

IV. SIMULATION DETAILS

We performed nonequilibrium molecular dynamics (NEMD) simulations for a Weeks–Chandler–Andersen (WCA) atomic fluid²⁶ undergoing planar Poiseuille flow. The algorithm for Poiseuille flow has been described in detail in several other publications^{24,27} and so we give here only a brief outline of the scheme employed.

The slit-pore model consists of a single wall comprising three layers of atoms arranged in an FCC lattice. The atoms in each layer are confined to their equilibrium sites through harmonic restraining forces; the layers themselves are subject to holonomic constraints which act to prevent their centers of mass from moving in the transverse direction. This model for pore walls was suggested by Powles.²⁸ Periodic boundary conditions were applied in all three Cartesian directions so that only one wall is needed per simulation cell to

represent a slit pore. We performed simulations at three different reduced pore widths: $L/\sigma=5.1, 10.2$, and 15.3 , where the pore width, L , is defined as the distance between the centers of mass of the two innermost opposing wall layers (throughout the remainder of this paper all quantities are given in reduced units defined in terms of the LJ energy and distance parameters).

Our coordinate system is defined such that the walls are parallel to the xz plane and the fluid is therefore confined in the y direction. To generate Poiseuille flow, we apply a constant force (pressure head) in the positive x direction to all fluid atoms which has the same desired effect as applying a pressure gradient without the undesirable complication of density gradients in the flow direction which would result from it. The magnitude of the pressure head used in this work was $F_e=0.02$ for all systems studied. This value was chosen to maximize the signal to noise ratio while maintaining a linear response. Typically, lower values of F_e may be used for wider pore widths but we found it convenient to retain a single value for all simulations.

In all our simulations, the number of wall atoms was fixed at 216 (72 atoms per layer). The number of fluid atoms differed, depending on the value of the pore width: 216, 504, and 864 for $L=5.1, 10.2$, and 15.3 , respectively. For each channel width we simulated fluid densities equal to 0.442 and 0.650, with a constant wall density for all systems of 0.850. We note that there is no unambiguous definition of volume in a pore system.²⁴ In this work we have defined the volume to be $V=(L-1)L_{x,z}^2$. The geometry of the overall system and walls is indicated in Fig. 1.

The equations of motion for the wall and fluid atoms were integrated using a fifth order Gear algorithm with a time step of 0.001. The magnitude of the spring constant for the wall atoms was chosen to be 57.1. This value was chosen to maximize the thermal coupling between the wall and fluid atoms, but we note that this relatively low value permits some penetration of the walls by fluid atoms. A Gaussian thermostat was applied to the wall atoms to maintain a constant kinetic wall temperature of 0.722 throughout the simulations. No thermostats are applied to the fluid; the viscous heat generated is allowed to dissipate via conduction through the walls.

Our simulations were conducted in the following manner. First, a pore of the appropriate dimensions was constructed and then filled with fluid atoms (the wall layers were simply replicated a certain number of times in the pore space). Second, the external field was applied and the system allowed to reach a nonequilibrium steady state (typically 1 million time steps). Production runs were then conducted for a duration of 400 million time steps. These extremely long runs were necessary in order to obtain the very high signal to noise values on the binned quantities. The shear stress was computed by integrating the momentum continuity equation (the so-called IMC method,²⁴ which involves integrating the density profile and multiplying by the external field magnitude) and the streaming velocity and density were collected in bins of small width.

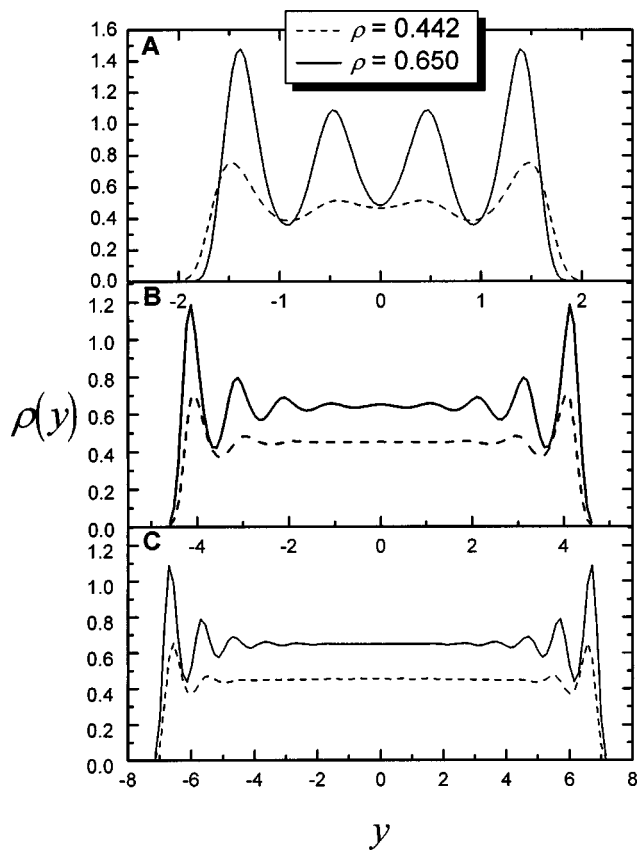


FIG. 2. Density $\rho(y)$ as a function of y for average fluid densities of $\rho=0.442$ (dashed line) and 0.650 (solid line). (A) $L=5.1$, (B) $L=10.2$, (C) $L=15.3$.

V. RESULTS AND DISCUSSION

In Fig. 2 the density $\rho(y)$ is plotted as a function of position for the three different channel widths. We note that $y=0$ represents the center of the fluid channel. As is to be expected the fluid is highly inhomogeneous for the smallest channel width ($L=5.1$) and experiences large density oscillations particularly in the layers immediately adjacent to both walls. These density oscillations are more pronounced for the higher average fluid density system ($\rho=0.650$) compared to the lower average density system ($\rho=0.442$). These oscillations become less significant towards the center of the channel as the channel size increases. For the $L=15.3$ system the only significant inhomogeneity appears in the immediate vicinity of the walls. The streaming velocity profiles are displayed in Fig. 3. For a classical Navier–Stokes fluid undergoing planar Poiseuille flow the streaming velocity profile should be quadratic in y , as demonstrated in Eq. (8). This is clearly not the case for the $L=5.1$ system, in which pronounced oscillations in the profile exist throughout the fluid, particularly for the higher density system. As the channel width increases these oscillations diminish near the center of the channel and are only significant close to the interface between wall and fluid atoms. The maximum streaming velocity decreases for fixed field strength as the channel width decreases due to increased frictional resistance between wall and fluid atoms. Figure 3 does show evidence of slip behavior, which is the subject of a separate paper currently in

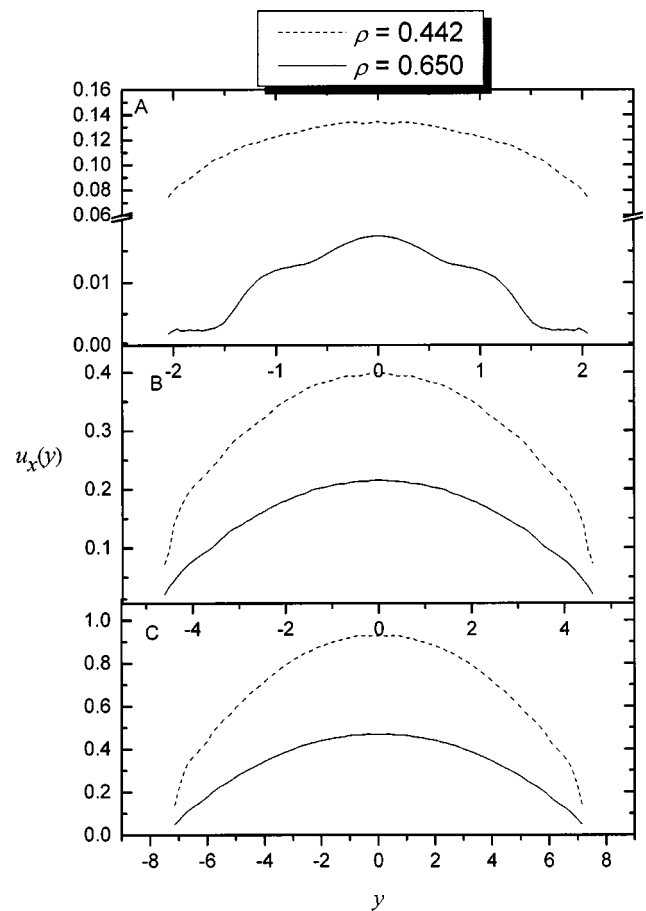


FIG. 3. Streaming velocity $u_x(y)$ as a function of y for average fluid densities of $\rho=0.442$ (dashed line) and 0.650 (solid line). (A) $L=5.1$, (B) $L=10.2$, (C) $L=15.3$.

preparation. The strain rate profiles for the same systems are shown in Fig. 4, where deviations from linearity are indicative of departures from Navier–Stokes predictions. As expected, these deviations are particularly pronounced for the $L=5.1$ system, again increasing in extent as the overall system density is increased from 0.442 to 0.650 . Linearity is only apparent for the $L=10.2$ and 15.3 systems sufficiently far removed from the walls. In Fig. 5 we plot $P_{yx}(y)$ as a function of y for all systems and again observe similar trends to those observed in Figs. 2–4, noting that deviations from the hydrodynamic linearity expected for Navier–Stokes fluids undergoing Poiseuille flow¹⁴ are manifest as strong oscillations in the vicinity of the walls, and that these oscillations increase in magnitude with increasing overall system density. In Fig. 6 we plot the real part of $\tilde{P}_{yx}(k_y)$, $\tilde{\gamma}(k_y)$, and $\tilde{\eta}(k_y)$ for a pore width of $L=15.3$.

We now make an observation in the calculation of the viscous kernel defined by Eq. (1). Let us add an arbitrary constant, η_0 , such that

$$\eta(\mathbf{r}-\mathbf{r}') = \eta_0 + \eta_1(\mathbf{r}-\mathbf{r}'). \quad (15)$$

Substitution of Eq. (15) into Eq. (1) yields in the zero frequency limit

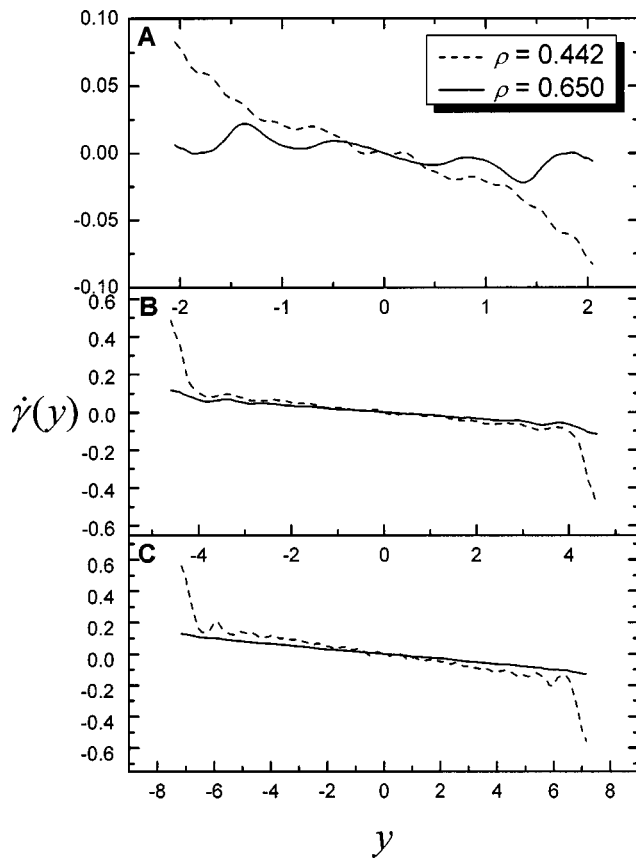


FIG. 4. Strain rate ($\dot{\gamma}$) as a function of y for average fluid densities of $\rho=0.442$ (dashed line) and 0.650 (solid line). (A) $L=5.1$, (B) $L=10.2$, (C) $L=15.3$.

$$P_{yx}(\mathbf{r}) = - \int_{-\infty}^{\infty} \eta_1(\mathbf{r}-\mathbf{r}') \dot{\gamma}(\mathbf{r}') d\mathbf{r}' - \eta_0 \int_{-\infty}^{\infty} \dot{\gamma}(\mathbf{r}') d\mathbf{r}'. \quad (16)$$

For planar Poiseuille flow we note that the second integral in Eq. (16) is zero. This would also be the case for *any* flow geometry in which the integral of the strain rate over all space is zero. Thus the contribution to the shear stress is *independent* of η_0 for our flow geometry. The viscous kernel defined by Eq. (1) is therefore only relative to some baseline value η_0 and this value needs to be determined. It cannot be determined simply by the Fourier transform method, which will only reconstruct η_1 . As η_0 defines a baseline viscosity, the SLLOD algorithm¹³ can be used to compute this baseline viscosity at a density, temperature, and strain rate that *match* the corresponding density, temperature, and strain rate near the middle of the channel where inhomogeneity is minimal (at the center of the channel $\dot{\gamma}=0$ so SLLOD cannot be used). In a previous paper²⁹ it was reported that “Only when inhomogeneity in the fluid causes significant nonlocal behavior can one expect measurable differences between the local properties of an SB (i.e., sliding boundary) simulation and the corresponding HS (i.e., SLLOD) values. This, for example, would be expected to be the case for the shear viscosity $\eta(\mathbf{r})$, where \mathbf{r} is located near the fluid-wall interface.” The extraction of this baseline viscosity and a viscosity from a viscous kernel will be the subject of a future publication. For now, we note that in what follows we compute the vis-

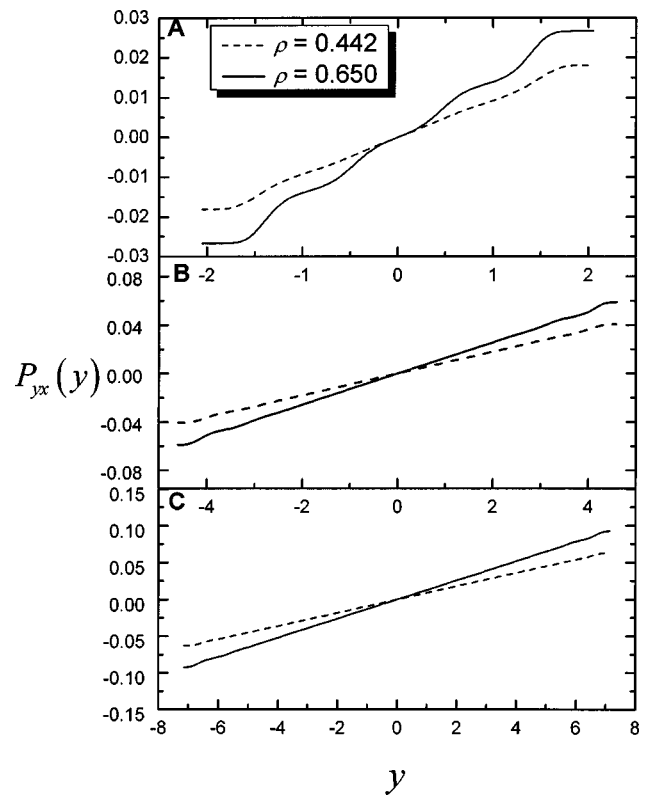


FIG. 5. Element of the pressure tensor $P_{yx}(y)$ computed by the IMC method (Ref. 24) as a function of y for average fluid densities of $\rho=0.442$ (dashed line) and 0.650 (solid line). (A) $L=5.1$, (B) $L=10.2$, (C) $L=15.3$.

cus kernel of Eq. (1), not the viscosity as is commonly defined by Eq. (6) for a homogeneous fluid. These two quantities have different units and are valid in terms of their defining constitutive relations [Eq. (1) for the viscous kernel and Eq. (6) for the viscosity].

In Figs. 7 and 8 we plot the viscosity and viscous kernel for all systems simulated. This includes Newton’s local viscosity defined by Eq. (6), and the Navier–Stokes viscosity for both densities studied. The viscous kernel is plotted on the same scale as the Newtonian and Navier–Stokes viscosities for comparison purposes only and should be interpreted only as a relative quantity on these plots. The Navier–Stokes viscosity is computed in the following way. We fit the streaming velocity simulation data to a parabolic function, $u_x(y) = c_2 y^2 + c_0$. Comparison of this function with the Navier–Stokes predicted velocity profile $u_x(y) = -(\rho F_e / 2 \eta_{NS})(y^2 - h^2)$ leads to the value $c_2 = -\rho F_e / 2 \eta_{NS}$, from which we compute the Navier–Stokes viscosity as $\eta_{NS} = -\rho F_e / 2 c_2$. There are several important conclusions that can be drawn from this comparison. First, it is clear that our viscous kernel does *not* suffer from the singularity problems clearly displayed by the local viscosity definition at $\dot{\gamma}=0$.^{14,15,30} This is dramatically observed for the high density $L=5.1$ system, where the local viscosity oscillates significantly throughout the channel and diverges to very large or even negative values near the stationary points in the streaming velocity profile where the strain rate goes to zero (which is, strictly speaking, undefined in the

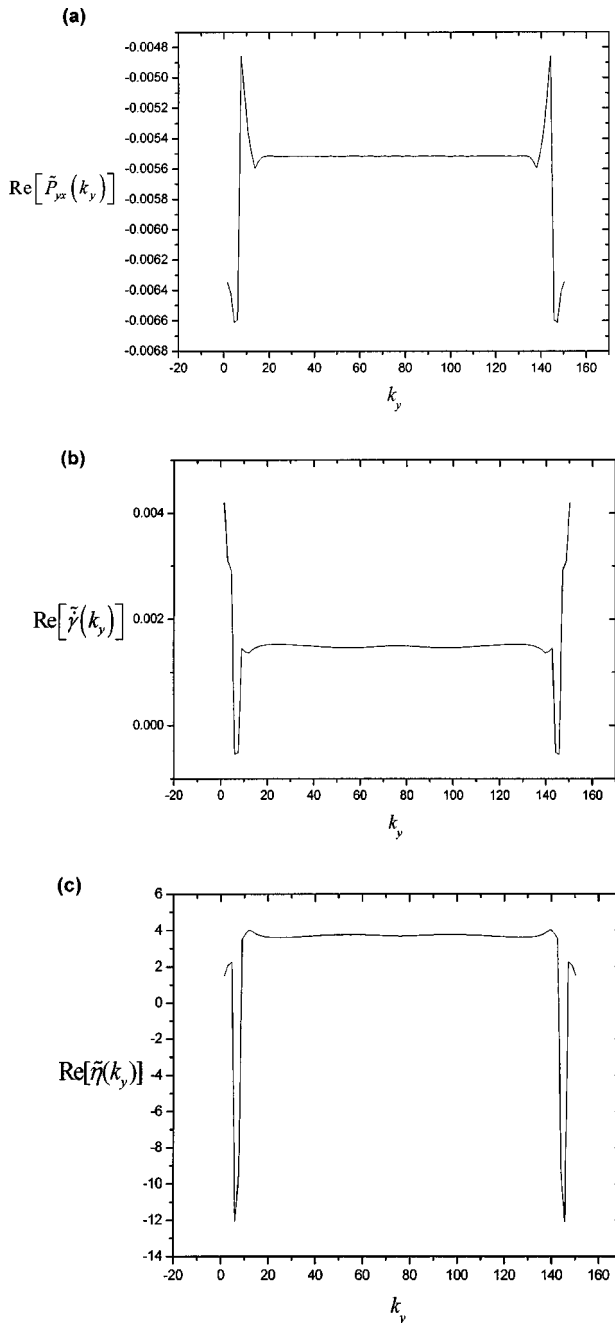


FIG. 6. k -space transforms of (a) shear stress, (b) strain rate, and (c) viscosity [Eq. (4)] for the system $L=15.3$ and $\rho=0.442$.

local model). In contrast, our viscous kernel behaves smoothly and suffers from no such singularity problems. It also demonstrates significantly improved statistical accuracy with typical standard errors of 1%–2% compared with 10%–15% for the local viscosity away from locations in the fluid where $\dot{\gamma} \rightarrow 0$. As is physically plausible, the viscous kernel does display strong oscillations near the walls that decay in strength towards the center of the channel. For the $L=10.2$ and 15.3 systems the viscous kernel is almost flat away from the walls, whereas the local viscosity demonstrates significant statistical fluctuations that cannot be physically real. The actual positions and numbers of peaks in the viscous kernel differ to those of the local viscosity, though as just

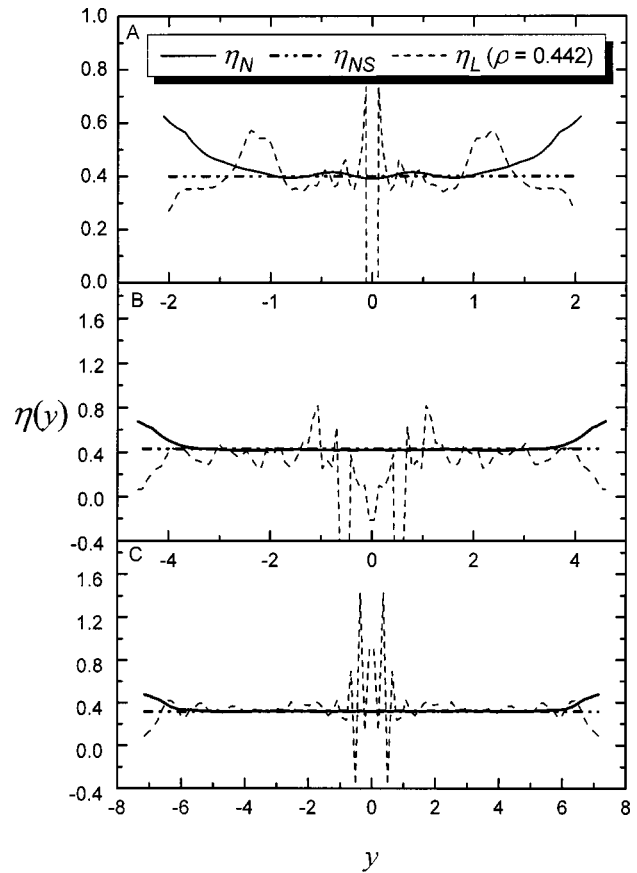


FIG. 7. Position dependent shear viscosities and viscous kernels as a function of y for an average fluid density of $\rho=0.442$. (A) $L=5.1$, (B) $L=10.2$, (C) $L=15.3$. $\eta_N(y)$ is computed by the nonlocal constitutive model, Eqs. (1)–(4); $\eta_L(y)$ is the local viscosity computed as $\langle -P_{yx}(y)/\dot{\gamma}(y) \rangle$, where $\langle \dots \rangle$ denotes a time average; $\eta_{NS}(y)$ is the Navier–Stokes shear viscosity computed as the ratio of shear stress to strain rate, where both quantities are assumed to have linear profiles as demanded by the Navier–Stokes solutions for a fluid undergoing planar Poiseuille flow. Typical errors are 1%–3% for $\eta_N(y)$ throughout the channel and 10%–15% for $\eta_L(y)$ away from stationary points in the streaming velocity profile where $\dot{\gamma}(y) \rightarrow 0$, but are not shown on the plot for visual clarity. Units of $\eta_N(y)$ are arbitrary.

pointed out the poor statistics for the local viscosities implies that many of these peaks are unphysical, particularly near the stationary points in the streaming velocity profile. Also shown are the Navier–Stokes viscosities which, by definition, are constant and thus incapable of predicting spatial variations in the viscosity for such highly inhomogeneous fluid systems. Nonetheless the invariance of the Navier–Stokes viscosities do agree reasonably well with relative invariance of the viscous kernels for the $L=10.2$ and 15.3 systems away from the walls, suggesting that the departure from hydrodynamic behavior really is only very significant in the first few atomic layers near the walls. Significantly, the statistical inaccuracy in the local viscosity measurements makes a similar comparison between the Navier–Stokes viscosity unreliable.

In order to confirm that the viscosity defined by Eq. (1) is consistent with that definition, we computed the stress from Eq. (1), using as input the viscous kernel computed from Eqs. (4), (12), (13) and the strain rate data. Excellent

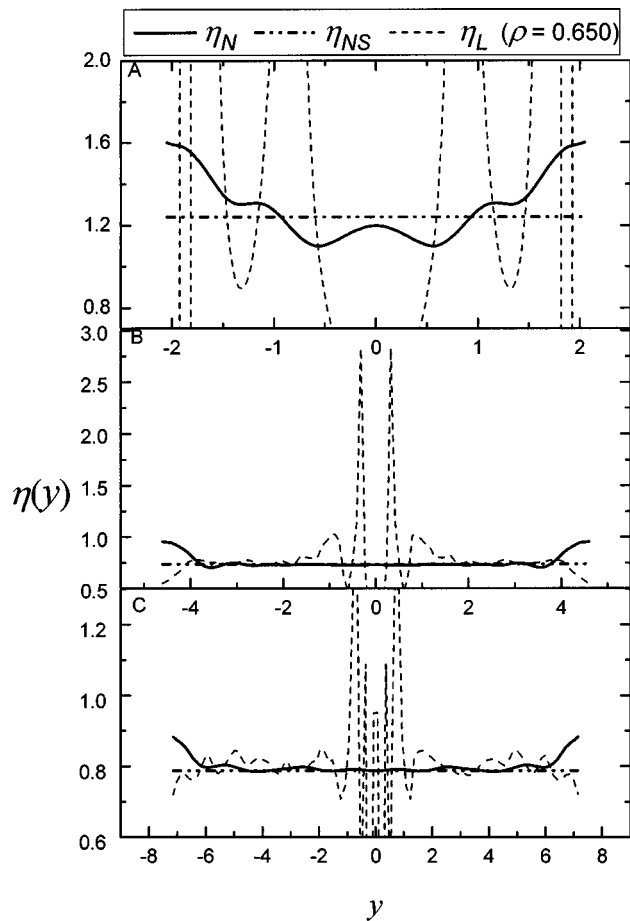


FIG. 8. Position dependent shear viscosities and viscous kernel as a function of y for an average fluid density of $\rho=0.650$. (A) $L=5.1$, (B) $L=10.2$, (C) $L=15.3$. Viscosities are as defined in Fig. 7. Typical errors are as indicated in Fig. 7.

agreement was found between both stress values, confirming the validity of our numerical procedure.

VI. PREDICTION OF FLOW PROFILES

Apart from fundamental studies of the \mathbf{k} -space dependence of the shear viscosity, our approach has potential for practical application in combined micro/mesoscale fluid simulations. In particular, from a fluid dynamics perspective, one is always interested in predicting flow profiles for complex geometries. In order to solve the Navier–Stokes equation for the streaming velocity one must make assumptions about the fluid’s viscosity. It is clear from Eq. (1) that the viscosity is a complex function of density, temperature and strain rate. It is thus not possible to extract a viscous kernel from Eq. (1) for a simple flow geometry and then use it to exactly solve for the flow profile in a more complex flow geometry because the density, temperature and strain rates in both types of flows will be different. However, in the weak field linear regime one might be able to solve this approximately. For example, our Poiseuille flow simulations could be used to extract a zero field spatially dependent viscosity, by running simulations at a number of field strengths and extrapolating to zero field. This viscous function represents a material property of the fluid at equilibrium. One could then

use this function for any arbitrary flow geometry in the weak field limit to obtain approximate flow profiles. To illustrate this idea, in what follows we describe how to predict the flow profile for planar Couette flow, making the assumption that in the weak flow limit the viscosity profiles for planar Poiseuille and Couette flows are similar.

The momentum continuity equation for any flow arbitrarily far from equilibrium is given as

$$\rho(\mathbf{r},t) \frac{d\mathbf{u}(\mathbf{r},t)}{dt} = -\nabla \cdot \mathbf{P}(\mathbf{r},t) + \rho(\mathbf{r},t)\mathbf{F}_e, \quad (17)$$

where \mathbf{F}_e is an external driving field per unit mass. Now, for the system to be in mechanical equilibrium there is no net acceleration of any fluid element so the left-hand side of Eq. (17) is identically zero. For planar Couette flow the external field is also zero, the flow being generated entirely by the moving wall boundaries. If our geometry is such that the two walls are moving with equal and opposite constant velocities in the x direction and the velocity gradient is in the y direction, then Eq. (17) reduces to

$$\frac{dP_{yx}(y,t)}{dy} = 0. \quad (18)$$

This implies that for planar Couette flow, no matter how strong the density inhomogeneities are in the system (e.g., flow in nanoporous materials), the shear stress will always have a constant value, unlike Poiseuille flow, where the shear stress demonstrates significant oscillations near the walls. In \mathbf{k} space, Eq. (18) becomes

$$\tilde{P}_{yx}(k_y) = 2\pi P_{yx} \delta(k_y), \quad (19)$$

where P_{yx} is a constant (the negative of the shear stress) and we drop the explicit t dependence in the equations since we deal with steady-state systems. Substituting Eq. (4) into the left-hand side of Eq. (19) gives

$$\tilde{\gamma}(k_y) = -\frac{2\pi P_{yx} \delta(k_y)}{\tilde{\eta}(k_y)}. \quad (20)$$

Thus, all that remains is to substitute in the \mathbf{k} -space viscosity profile (obtained from our Poiseuille flow simulations) into Eq. (20) and then take the inverse Fourier transform to obtain the flow profile, i.e.,

$$u_x(y) = \frac{1}{2\pi} \int dy \int_{-\infty}^{\infty} dk_y \tilde{\gamma}(k_y) e^{ik_y y}. \quad (21)$$

We further note that the shear stress P_{yx} is easily obtained as the ratio of the total force on the shearing boundary layer (i.e., the moving wall) to the surface area of the wall. An examination of Eq. (20) immediately tells us that the flow profile for planar Couette flow will depart from the linear prediction of Navier–Stokes theory and will contain oscillations dependent on the spatially varying viscosity profile. Furthermore Eq. (21) is independent of η_0 . All we need is the \mathbf{k} -space viscosity, making a determination of η_0 from alternative approximate methods unnecessary.

To demonstrate that this procedure works, we predict the flow profile for an atomic fluid of WCA particles undergoing planar Couette flow with a channel width of $L=5.1$. We use

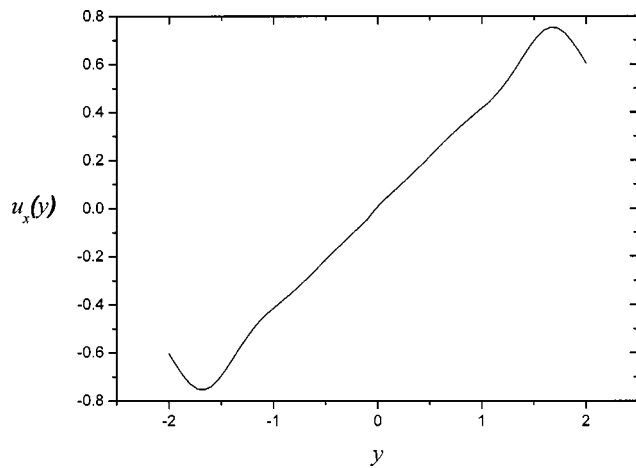


FIG. 9. Predicted flow profile for planar Couette flow for a pore of width $L=5.1$ and fluid density $\rho=0.442$. Flow velocity units are arbitrary.

the viscosity profiles computed for the $L=5.1$ system undergoing planar Poiseuille flow with a fluid density of 0.442 with a field strength of $F_e=0.02$ as before. Substituting the \mathbf{k} -space viscosity profile into Eq. (21) above leads to the predicted flow profile in Fig. 9, where we note that the units are arbitrary. The arbitrariness of the units is due solely to the fact that we do not have a simulated shear stress $-P_{yx}$ for this system, which we justify because our intention in this paper is to demonstrate the method rather than make specific quantitative calculations. The flow profile in Fig. 9 is what is to be expected: almost linear near the center of the channel with significant oscillations superposed towards the walls, in qualitative agreement with the simulation results of Bitsanis *et al.*⁶ despite the assumption that the viscous kernel represents an effective “density averaged” viscosity density. We stress again that the viscosities for Couette and Poiseuille flows are *not* expected to be the same outside of the weak flow linear regime, and therefore its use in the prediction of flow fields for alternative flow geometries needs to be tackled cautiously. Indeed, this was noted in the work of Bitsanis *et al.*^{6–8} who found significant differences in the effective viscosities computed with their local average density model for both types of flow.

VII. CONCLUSIONS

We have used the nonlocal linear constitutive model proposed by Evans and Morriss¹³ to compute the effective position dependent viscosity kernel and applied it to a confined fluid undergoing planar Poiseuille flow. While approximate in the sense that explicit density dependence is excluded, the method does not suffer from singularities obtained from using effective local viscosities and demonstrates how poor an approximation Newton’s law of viscosity is for nanofluids. We anticipate that such a position dependent viscosity can be useful in the study of nanofluidics, without the need for limiting approximations about locality, or other heuristic approximations. Our viscous kernel is *defined* for nonequilibrium flows and is based on a hydrodynamic definition, unlike for example the Pozhar–Gubbins viscosity that is strictly

valid close to equilibrium and is based upon kinetic theory approximations. It is simple to compute and does not require any assumptions other than a determination of the baseline viscosity. As experimental measurements of the position dependent viscosity for such highly inhomogeneous systems are currently unavailable, computer simulation remains the most accessible means to determine the transport coefficients for these technologically important fluid systems. Furthermore, we have demonstrated how to use such a viscous kernel to obtain approximate streaming velocity profiles for arbitrary flow geometries in the weak linear regime. This approach may be useful for the study of nanoscale flows by methods that combine microscopic and mesoscopic simulation methods.

ACKNOWLEDGMENTS

The authors thank Professor Denis Evans for a useful discussion during the course of this work. The authors also thank the Australian Partnership for Advanced Computing (APAC) for a generous allocation of computing time. One of the authors (K.P.T.) thanks the School of Information Technology, Swinburne University, for a Visiting Fellowship. The first author (J.Z.) thanks the Australian Government for financial assistance.

- ¹H. T. Davis, *J. Chem. Phys.* **86**, 1474 (1987).
- ²H. T. Davis, *Chem. Eng. Commun.* **58**, 413 (1987).
- ³T. K. Vanderlick and H. T. Davis, *J. Chem. Phys.* **87**, 1792 (1987).
- ⁴S. A. Somers and H. T. Davis, *J. Chem. Phys.* **96**, 5389 (1992).
- ⁵W. T. Ashurst and W. G. Hoover, *Phys. Rev. A* **11**, 658 (1975).
- ⁶I. Bitsanis, J. J. Magda, M. Tirell, and H. T. Davis, *J. Chem. Phys.* **87**, 1733 (1987).
- ⁷I. Bitsanis, T. K. Vanderlick, M. Tirell, and H. T. Davis, *J. Chem. Phys.* **89**, 3152 (1988).
- ⁸I. Bitsanis, S. A. Somers, H. T. Davis, and M. Tirell, *J. Chem. Phys.* **93**, 3427 (1990).
- ⁹S. Y. Liem, D. Brown, and J. H. R. Clarke, *Phys. Rev. A* **45**, 3706 (1992).
- ¹⁰A. Baranyai, D. J. Evans, and P. J. Daivis, *Phys. Rev. A* **46**, 7593 (1992).
- ¹¹B. D. Todd and D. J. Evans, *Phys. Rev. E* **55**, 2800 (1997).
- ¹²P. J. Daivis and J. L. Khayyam Coelho, *Phys. Rev. E* **61**, 6003 (2000).
- ¹³D. J. Evans and G. P. Morriss, *Statistical Mechanics of Nonequilibrium Liquids* (Academic, London, 1990).
- ¹⁴K. P. Travis, B. D. Todd, and D. J. Evans, *Phys. Rev. E* **55**, 4288 (1997).
- ¹⁵K. P. Travis and K. E. Gubbins, *J. Chem. Phys.* **112**, 1984 (2000).
- ¹⁶H. W. Hu, G. A. Carson, and S. Granick, *Phys. Rev. Lett.* **66**, 2758 (1991); S. Granick, *Science* **253**, 1374 (1991); J. Klein and E. Kumacheva, *ibid.* **269**, 816 (1995).
- ¹⁷L. A. Pozhar and K. E. Gubbins, *J. Chem. Phys.* **94**, 1367 (1991).
- ¹⁸L. A. Pozhar and K. E. Gubbins, *J. Chem. Phys.* **99**, 8970 (1993).
- ¹⁹L. A. Pozhar, *Transport Theory of Inhomogeneous Fluids* (World Scientific, Singapore, 1994).
- ²⁰W. Sung and J. S. Dahler, *J. Chem. Phys.* **80**, 3025 (1984).
- ²¹E. Akhmatkaya, B. D. Todd, P. J. Daivis, D. J. Evans, K. E. Gubbins, and L. A. Pozhar, *J. Chem. Phys.* **106**, 4684 (1997).
- ²²J. P. Hansen and I. R. McDonald, *Theory of Simple Liquids* (Academic, New York, 1986).
- ²³K. P. Travis, D. J. Searles, and D. J. Evans, *Mol. Phys.* **97**, 415 (1999).
- ²⁴B. D. Todd, D. J. Evans, and P. J. Daivis, *Phys. Rev. E* **52**, 1627 (1995).
- ²⁵P. V. O’Neil, *Advanced Engineering Mathematics* (Wadsworth, California, 1983).
- ²⁶J. D. Weeks, D. Chandler, and H. C. Andersen, *J. Chem. Phys.* **54**, 5237 (1971).
- ²⁷B. D. Todd, P. J. Daivis, and D. J. Evans, *Phys. Rev. E* **51**, 4362 (1995).
- ²⁸J. G. Powles, S. Murad, and P. V. Ravi, *Chem. Phys. Lett.* **188**, 21 (1992).
- ²⁹B. D. Todd, D. J. Evans, K. P. Travis, and P. J. Daivis, *J. Chem. Phys.* **111**, 10730 (1999).
- ³⁰L. A. Pozhar, *Phys. Rev. E* **61**, 1432 (2000).